
DOPPLER-ASSISTED QUANTUM RESONANCES THROUGH SWAPPABLE EXCITATION PATHWAYS IN POTASSIUM VAPOR

Gourab Pal

Raman Research Institute
Bangalore, India
gourab@rrimail.rrri.res.in

Subhasish Dutta Gupta

TIFR Hyderabad, IISER Kolkata
IIT Jodhpur
sdghyderabad@gmail.com

Saptarishi Chaudhuri

Raman Research Institute
Bangalore, India
srishic@rrri.res.in

March 28, 2024

ABSTRACT

We report the observation of two additional sub-natural line width quantum interference in the D_2 manifold of ^{39}K vapor, in addition to the usual single Electromagnetically induced transparency peak. The other two features appear exclusively because ^{39}K ground hyperfine splitting is smaller than the Doppler broadened absorption profile. This allows probe and control beams to swap their transition pathways. The control beam detuning captures the nature of the coherence, therefore an unusual phenomenon of conversion from perfect transparency to enhanced absorption is observed and explained by utilizing adiabatic elimination of the excited state in the Master equation. Controlling such dark and bright resonances leads to new applications in quantum technologies viz. frequency offset laser stabilization and long-lived quantum memory.

1 Introduction

For the past few decades, manipulating and controlling an atomic medium's optical responses [1] using quantum interference across excitation channels has been a versatile field of study. One of the most fascinating quantum interference phenomena is electromagnetically-induced transparency (EIT) [2, 3, 4], which modifies the medium's dispersion characteristics dramatically and opens the door to several cutting-edge uses in quantum information processing [5], including the creation of high-precision quantum sensors [6], atomic clocks [7], magnetometers [7], etc. As an application to quantum memory [8], it is feasible to slow down [9] or store photons [10] for a considerable time due to the steep anomalous dispersion in an EIT medium. The

EIT medium can be used for creating entangled bi-photons[11] having application in quantum communication. More recently, exotic effects Goos-Hänchen [12], and Imbert-Fedorov shifts [13] have been observed employing EIT medium.

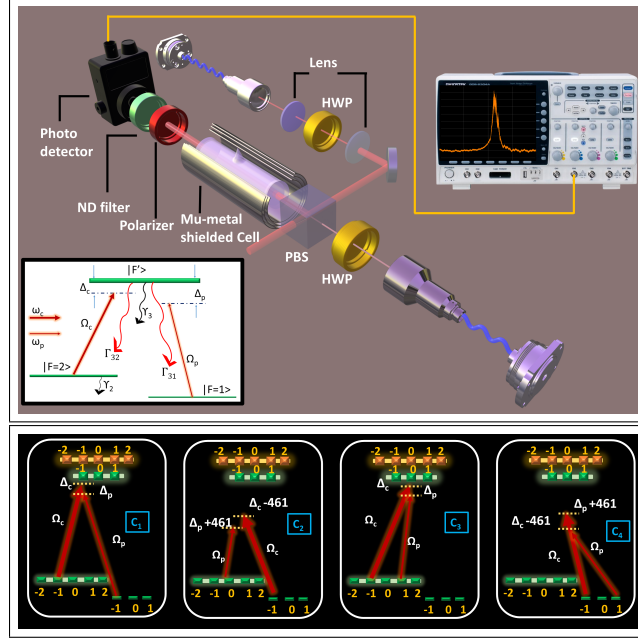


Figure 1: (Up) Schematic of experimental setup. Essential optical components are labeled in the figure. The inset shows a typical three levels Λ -system with relevant parameters. (Down) All four Λ -type configurations are supported due to small ground state splitting (see text) in ^{39}K atomic ensemble. Here ground states are $|F = 1\rangle$ (indicated by a thin line) and $|F = 2\rangle$ (indicated by a relatively thick line). (color online)

Numerous experiments have been carried out in diverse atomic systems such as ^{87}Rb [14], ^{133}Cs [15], ^{23}Na [16], metastable He [17], Erbium-doped fiber [18], molecular Lithium [19], EIT with Rydberg atoms [20, 21]. These systems exhibit strong quantum interference phenomena (like EIT) due to their wide ground state separation and considerable energy spacing among excited states. Furthermore, in a typical atomic vapor, the Doppler broadening is much smaller than the ground state separation, leading to the observation of just one EIT peak. On the other hand, the ground state separation in ^{39}K is smaller (461.7MHz [22]) than the Doppler broadening at room temperature which makes the study of EIT in ^{39}K intriguing. There exist very few quantum interference-based experiments in ^{39}K , Long et.al. [23] used a chirped waveform electro-optic modulator to investigate the EIT, A. Sargsyan et al. [24] demonstrated on-resonance EIT and Gozzini et.al [25] observed EIT-EIA transition in Hanle configuration with polarization as a tuning parameter. In this article, we experimentally demonstrate the emergence of three distinct quantum interference line shapes in a Λ -type system in ^{39}K atomic ensemble. The ground-state hyperfine splitting being smaller than the unresolved two overlapping Doppler absorption profiles, the excitation pathways of the control and probe beam can be swapped. We also observe a transition from complete transparency to enhanced absorption as we vary

the control beam detuning from the blue side to the red side of its resonance point, while the two-photon detuning condition is satisfied.

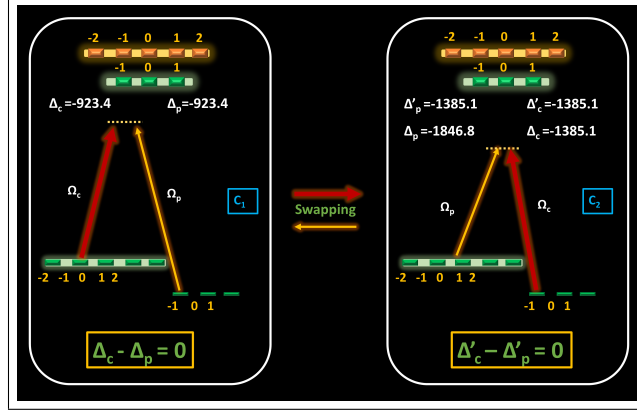


Figure 2: (Left) The usual case C_1 with two-photon detuning $\Delta_c - \Delta_p = 0$. (Right) Control and probe transition pathways are swapped. In the swapped frame (case C_2), $\Delta'_c - \Delta'_p = 0$. See text for details. (color online)

2 Experimental setup and methods

Figure 1 (Upper panel) shows a schematic of the experiment. Two independent grating stabilized diode lasers (Toptica DL Pro and DL100) are used as the control and probe beam. The probe and control lasers are tuned near $F=1$ to F' and $F=2$ to F' respectively in the D_2 manifold of ^{39}K , with a typical laser line width of 1MHz. Two separate acousto-optic modulators are used to independently control the intensity and detuning of the probe and control beams. The frequency reference is obtained using two saturated absorption spectroscopy, see supplementary [26]. A 75 mm long and 25mm diameter spectroscopy-grade commercial vapor cell containing ^{39}K (in natural abundance, $\sim 93\%$) is placed inside a three-layered μ -metal jacket to efficiently shield any stray magnetic field. The probe beam and control beams are mode-filtered using single mode polarization maintaining fibers and passed through two independent telescopic arrangements with exit beam diameters of 1mm and 4mm, respectively. The two beams are prepared in orthogonal linear polarization states and merged using a polarizing beam splitter cube before being sent to the atoms. The probe laser is kept in frequency scan mode whereas the control laser frequency is kept at various detunings. In the end, the control beam is filtered out using a linear polarizer (extinction ratio $1 : 10^5$), and the signal is obtained using a photo-detector (Thorlabs PDA10A2) with 150MHz bandwidth. A high-speed oscilloscope (2Gs/sec) is used for visualization and data recording.

3 Theoretical description

A semi-classical approach with density matrix formalism is applied to this three-level Λ system as shown in the inset of figure 1 (Upper panel). The two ground states are $|F=1\rangle$ and $|F=2\rangle$ hyperfine levels in $^2S_{1/2}$ and the excited state is taken as unresolved $|F'\rangle$ in $^2P_{3/2}$ containing

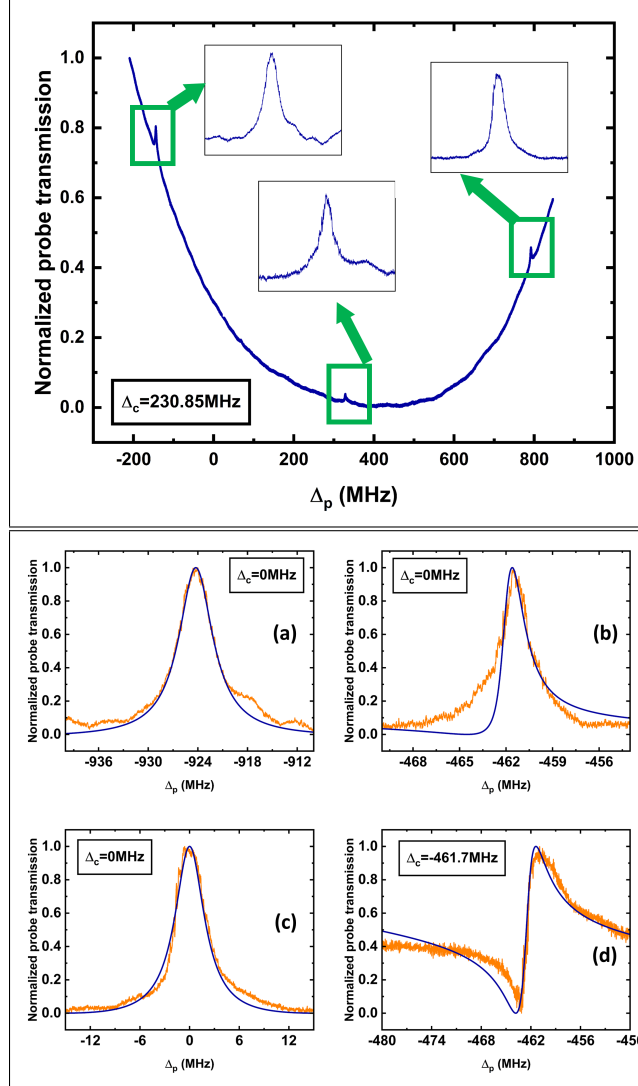


Figure 3: (Upper panel) Observation of three bright resonances for $\Delta_c = 230.85$ MHz. The inset shows the zoomed views. (Lower panel) On-resonant ($\Delta_c = 0$) bright resonance line shapes (a,b,c). The orange line indicates experimental data and the blue line is the theoretical model fit. Subplot (d) shows the admixture of dark and bright resonance at $\Delta_p = -461.7$ MHz. (color online)

$F'=0,1,2$ and 3 states. The Master equation that governs the dynamics of a mixed state is, $\dot{\rho} = -\frac{i}{\hbar}[H, \rho] + \mathcal{L}\rho$. Here ρ is the density matrix of the system, and H is the EIT Hamiltonian [3]. The last term $\mathcal{L}\rho$, is the pertinent Lindbladian term that controls all potential decay processes such as leaky transitions from other excited states, spontaneous emission, and decoherence resulting from Doppler-broadening. Such decay terms account for the interactions with the environment and thus make the system's dynamics non-unitary. In our case, the dominant decay processes are due to Doppler broadened spontaneous emission and energy-conserving dephasing effects like collision of atoms with walls, and atom-atom collisions.

The non-unitary Lindbladian term, see supplementary [26], is $\mathcal{L}\rho = \Gamma_{31}\mathcal{D}[\hat{\sigma}_{1,3}]\rho + \Gamma_{32}\mathcal{D}[\hat{\sigma}_{2,3}]\rho + \gamma_2\mathcal{D}[\hat{\sigma}_{2,2}]\rho + \gamma_3\mathcal{D}[\hat{\sigma}_{3,3}]\rho$, where Γ_{ij} denotes spontaneous decay rate from state i to state j , γ_i is a energy-conserving dephasing term for state i , $\hat{\sigma}_{i,j}$ is a jump operator defined as $\hat{\sigma}_{i,j} = |i\rangle\langle j|$ and \mathcal{D} is coined as Lindblad super-operator whose action is defined as $\mathcal{D}[A]B = ABA^\dagger - \frac{1}{2}\{A^\dagger A, B\}$ for any two operators A and B . In light of such formalism, the susceptibility seen by the probe $\chi(\omega_p)$ can be obtained by solving coherence terms under steady-state conditions as,

$$\chi(\omega_p) = \frac{2n|d_{13}|}{\epsilon_0 E_p} \frac{\Omega_p [2i\Delta + \gamma_2]}{-4i\Delta_p\Delta + i\Omega_c^2 - 2\Delta_p\gamma_2 + i\Gamma_3 [2i\Delta + \gamma_2]} \quad (1)$$

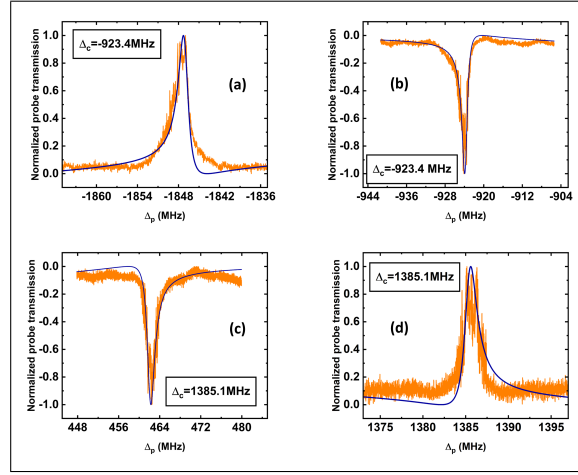


Figure 4: (Upper panel) In the red-side of control beam resonance, subplot a shows complete transparency due to case C_2 , subplot b shows full absorption due to case C_1 . (Lower panel) The opposite parity line shapes are seen with blue-detuned control light as shown in subplot c and d.

Here, n is the density of atoms at cell temperature T , $|d_{13}|$ is the dipole matrix element, E_p is probe field amplitude, $\Gamma_3 = \Gamma_{32} + \Gamma_{31} + \gamma_3$ is the total decoherence of excited state, γ_2 indicates ground state decoherence, γ_3 is excited state energy conserving decoherence, Ω_p , Ω_c are probe and control Rabi flopping frequencies, respectively and Δ_p , Δ_c and $\Delta = \Delta_p - \Delta_c$, are respective probe detuning, control detuning and two-photon detuning from a given transition (see figure 1).

4 Results and discussions

The ground state splitting of the Potassium atom is 461.7 MHz which is smaller than the unresolved two Doppler broadened absorption profiles (684 MHz [26] at a cell temperature of 60°C). Under this circumstance, the usual EIT peak with $\Delta_c = 0$ is observed which is the standard case C_1 in figure 1. However, since there exists a significant number of atoms with velocities such that a Doppler shift can be higher than ground-state hyperfine splitting, the excitation pathways of the control and probe beam can now be swapped. The swapping mechanism is illustrated in figure 2 where, as an example, $\Delta_c = -923.4$ MHz is taken. Before swapping, $\Delta_c = \Delta_p = -923.4$ MHz, so the two-photon detuning is satisfied. However after swapping, $\Delta'_c = \Delta_c - 461.7 = -1385.1$ and $\Delta'_p = \Delta_p + 461.7$. Since the probe laser is scanning,

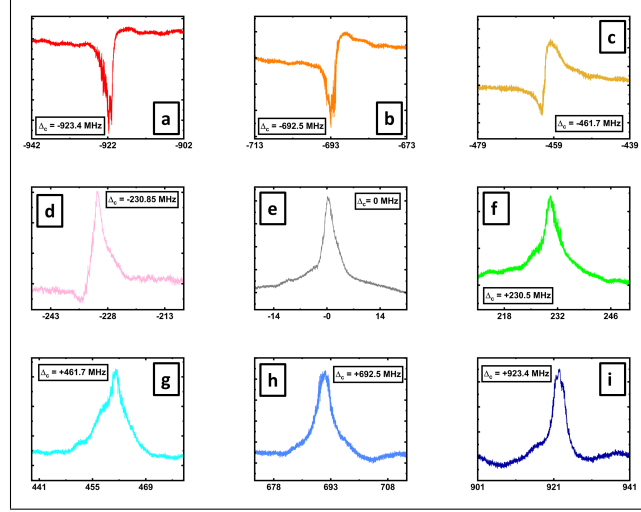


Figure 5: Transition from bright resonance to dark resonance as we vary the control detuning for the case C_1 . The x-axis is the probe detuning, y-axis represents probe transmission. Inset-box shows the corresponding Δ_c values. (color online)

the probe frequency is adjusted to $\Delta_p = -1846.8$ so that $\Delta'_p = -1385.1$ and the two-photon detuning condition is satisfied in this swapped frame. A third line shape is obtained by applying the same arguments but with control and probe beam making a valid Λ from the same hyperfine state either $|2\rangle$ (for the case C_3) or $|1\rangle$ (for the case C_4) [26]. See figure 1 (lower panel) for all four possible configurations. There are multiple Λ -system within a given case, considering all possible magnetic sublevels. We have considered all such transition probabilities with their corresponding Clebs-Gordan coefficients. The resulting line shapes and their positions remain largely unaffected as discussed in [26].

As a representative dataset, figure 3 (Upper panel) shows all three EIT line shapes riding on the Doppler broadened absorption profile, here the control detuning is set to $\Delta_c = 230.85$ MHz. The corresponding background-subtracted features are zoomed in the insets. The relevant physics is well captured by introducing correct dephasing terms. The figures (a,b,c) in figure 3 (lower panel) show all possible bright resonances with corresponding theoretical model fit. The subplot (c) is the usual single EIT peak, which is also observed in other atoms like Rb, Cs, etc. The characteristic variation of EIT line width with Ω_c for the case of $\Delta_c = -923.4$ MHz is also studied with theoretical fitting (see supplementary [26]) as presented in the susceptibility expression. The inclusion of an overlapping Doppler broadened profile enables us to exchange the excitation pathways of control and probe which give two additional features (a and b). The asymmetric mismatch between theory and experiment is accounted for non-zero probe detuning and the existence of multiple excited states [27, 28] in the case of ^{39}K . The asymmetry primarily originates from the admixture of pure dark state and pure bright state as can be seen in subplot (d) of figure 2 where the dip is observed due to bright resonance and the peak is due to dark resonance.

When the control beam detuning is taken to far-off red detuned, $\Delta_c = -923.4$ MHz, a complete absorption and complete transmission line shapes are observed at probe detunings $\Delta_p =$

-923.4MHz and $\Delta_p = -1846.8\text{MHz}$ respectively. For blue-detuning, $\Delta_c = 1385.1\text{MHz}$, complete absorption, and transmission are seen in $\Delta_p = 461.7\text{MHz}$ and $\Delta_p = 1385.1\text{MHz}$ respectively as shown in figure 4. For the cases of far-off resonant complete absorption, we have adiabatically eliminated [29] the state $|F'\rangle$ from the Master equation to get the correct line shape by switching off the spontaneous decay in the Lindblad term. This is a reasonable description because, at far-off resonance from the one-photon transition the lasers do not significantly populate the excited state thereby reducing the spontaneous decay from the excited state. The theoretical model fit gives effective γ_2 values ranging from 1.2 MHz to 2.5 MHz depending on the line shape position. The other variable parameters $\gamma_3, \Gamma_{31}, \Gamma_{32}$ are adjusted according to the probe and control detunings. For a given line shape, if it appears inside the Doppler, then the dephasing will be controlled by the spontaneous decay term and if it appears outside the Doppler, then the dephasing will come primarily from γ_3 . As an example, for $\Delta_c = -923.4\text{MHz}$ (case C_3), the values of $\gamma_2 = 1.2\text{MHz}$, $\Gamma_{31} = \Gamma_{32} = 0$ and $\gamma_3 = 342\text{MHz}$.

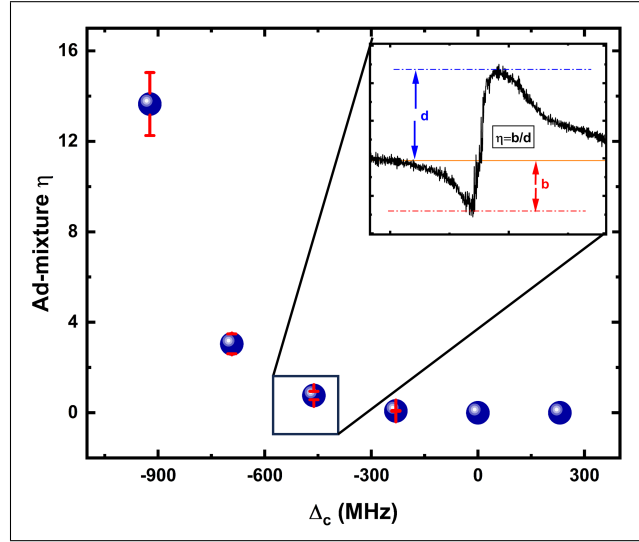


Figure 6: Ad-mixture parameter η as a function of control detuning Δ_c . As Δ_c is swept from the red side to the blue side, complete transparency is obtained due to the formation of dark resonance, consequently, the bright state ad-mixture parameter η vanishes after $\Delta_c \geq 0$.

Figure 5 (a-i) shows a transition from bright resonance to dark resonance as we vary the control beam detuning keeping the probe laser scanning across the whole D_2 manifold. The blue side of this case always gives bright resonance as can be seen from (f-i) of figure 5. The line-plot colors are chosen to represent the detuning of the control beam. These line shapes are obtained for the case C_1 . A similar transition can be found in other cases also. To indicate the extent of mixing of bright and dark resonance, the ad-mixing parameter η is defined as the ratio of bright resonance contrast (defined as b) and dark resonance contrast (defined as d). The variation of η is plotted against the control beam detuning which gave exponential crossover from bright resonance to dark resonance as we sweep the control beam detuning as shown in figure 6.

5 Conclusion and outlook

By choosing both the Doppler and exchanging the probe and control beam excitation routes, we have been able to explain all possible line shapes and positions and they match well with the density matrix formalism-based theoretical model. The adiabatic elimination works well to describe the bright resonance in blue as well as red detuning regions. The exact line shape can be matched by taking into account the intervention of other excited states as described in [30]. Going beyond the Gaussian probe and control, a probe beam carrying orbital angular momentum (Laguerre Gaussian mode) can have a fundamentally unique response [31] to this EIT medium because of the spatial variation of Rabi frequency that can lead to line shape narrowing [32] as well as change in asymmetries. Another novel avenue to explore EIT in Potassium will be to study cold Potassium atoms [33] in a strong magnetic field where the external magnetic field can couple the Zeeman sub-levels of different hyperfine states. The explanation of all these quantum interference line shapes enriches the understanding of quantum coherence and has applications to frequency-offset tight laser locking [34] and quantum technology applications such as optical isolators [35] quantum memory [8], slow light [36].

Appendices

A The Master equation

In the density matrix formalism, the Von Neumann equation governs the time evolution of mixed-state density matrix ρ

$$\dot{\rho} = -\frac{i}{\hbar}[H, \rho] \quad (2)$$

Here H is the EIT Hamiltonian [3] for our 3-level Λ system as described in the main text.

$$H = -\frac{i}{\hbar} \begin{bmatrix} 0 & 0 & \Omega_p \\ 0 & 2(\Delta_p - \Delta_c) & \Omega_c \\ \Omega_p & \Omega_c & 2\Delta_p \end{bmatrix} \quad (3)$$

In atomic systems, there are many decay processes such as spontaneous emission, dephasing, or decoherence due to inhomogeneous magnetic fields, ground state collisions, spin-exchange collisions, and so on. Such terms make the above Hamiltonian non-unitary. We can make a Lindblad term that needs to be added to the above Hamiltonian to correctly describe our present system. The irreversible Lindblad term can be written as

$$\mathcal{L}\rho = \Gamma_{31}\mathcal{D}[\hat{\sigma}_{1,3}]\rho + \Gamma_{32}\mathcal{D}[\hat{\sigma}_{2,3}]\rho + \gamma_2\mathcal{D}[\hat{\sigma}_{2,2}]\rho + \gamma_3\mathcal{D}[\hat{\sigma}_{3,3}]\rho \quad (4)$$

where Γ_{ij} denotes spontaneous decay from state i to state j , γ_i is a energy-conserving dephasing term for state i , $\hat{\sigma}_{i,j}$ is a jump operator defined as $\hat{\sigma}_{i,j} = |i\rangle\langle j|$ and \mathcal{D} is coined as Lindblad super-operator whose action is defined as $\mathcal{D}[A]B = ABA^\dagger - \frac{1}{2}\{A^\dagger A, B\}$ for any two operators

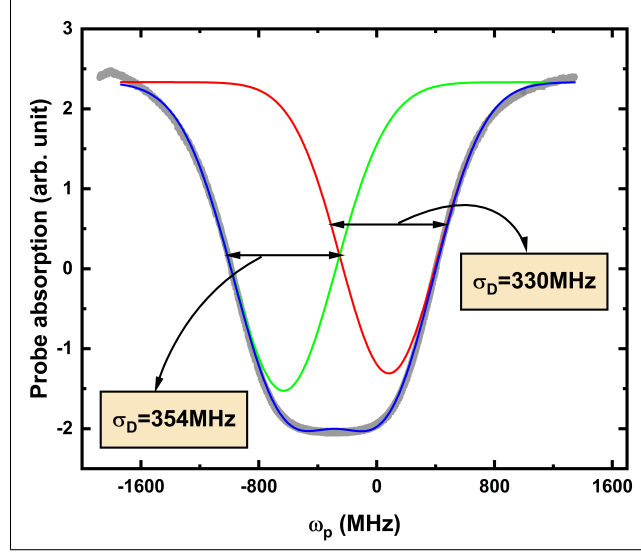


Figure 7: Representation of overlapping Doppler broadened absorption profiles. The thick grey line is the experimental data, the red and green are individual Doppler absorption fitted by Gaussian, and the blue line is the convolution of two Doppler. (color online)

A and B. Setting the basis as $\{[1, 0, 0]^T, [0, 1, 0]^T, [0, 0, 1]^T\}$, the jump operators can be easily constructed. Upon simplification, the Lindblad term becomes

$$\mathcal{L}\rho = -\frac{1}{2} \begin{bmatrix} 0 & \gamma_2\rho_{12} & (\Gamma_{31} + \Gamma_{32} + \gamma_3)\rho_{13} \\ \gamma_2\rho_{12}^* & 0 & (\Gamma_{31} + \Gamma_{32} + \gamma_3 + \gamma_2)\rho_{23} \\ (\Gamma_{31} + \Gamma_{32} + \gamma_3)\rho_{13}^* & (\Gamma_{31} + \Gamma_{32} + \gamma_3 + \gamma_2)\rho_{23}^* & 0 \end{bmatrix} \quad (5)$$

Here in ρ matrix, we need to set $\rho_{11} = 1$, $\rho_{22} = 0$ and $\rho_{33} = 0$.

B Steady state solution of coherence terms

After adding Lindbladian to the Von Neumann equation, we can read out two required coherence terms

$$\dot{\rho}_{12} = [-\frac{1}{2}\gamma_2 + i(\Delta_c - \Delta_p)]\rho_{12} - \frac{1}{2}i\Omega_c\rho_{13} \quad (6)$$

$$\dot{\rho}_{13} = [-\frac{1}{2}(\Gamma_{31} + \Gamma_{32} + \gamma_3) - i\Delta_p]\rho_{13} - \frac{1}{2}i\Omega_c\rho_{12} - \frac{1}{2}i\Omega_p \quad (7)$$

In steady state conditions, we can set $\dot{\rho}_{ij} = 0$, which gives two linear equations that can be solved analytically. The solution for ρ_{13} is directly related to the susceptibility seen by the probe.

$$\chi_p \sim \frac{\Omega_p[2i(\Delta_p - \Delta_c) + \gamma_2]}{-4i\Delta_p(\Delta_p - \Delta_c) + i\Omega_c^2 - 2\Delta_p\gamma_2 + i(\Gamma_{31} + \Gamma_{32} + \gamma_3)[2i(\Delta_p - \Delta_c) + \gamma_2]} \quad (8)$$

In the main text, we only plot the probe transmission in various detunings which is the imaginary part of $\chi(p)$.

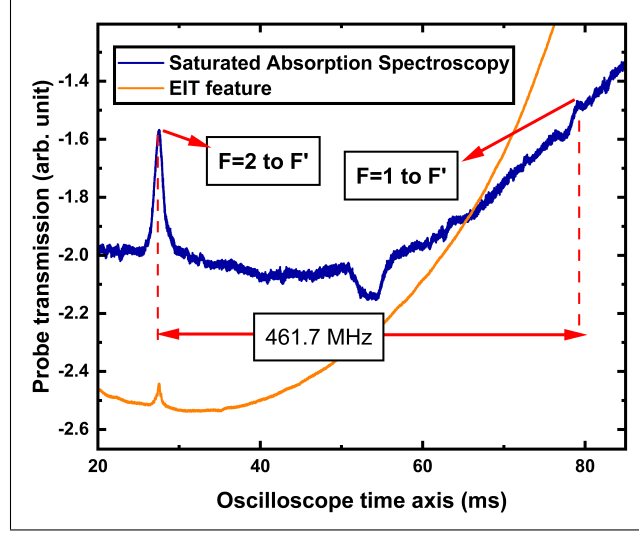


Figure 8: Saturated Absorption Spectroscopy of ^{39}K used for the conversion of time scales in oscilloscope to frequency scale.

C Overlapping Doppler broadened absorption profile in ^{39}K

The ground state hyperfine splitting is 461.7MHz. Now, at 333K, the Doppler width is 342 MHz, calculated using the formula $\sigma_D = \sqrt{\frac{k_B T}{m c^2}} \omega_p$, where k_B is Boltzmann constant, m is atomic mass, c is the velocity of light and ω_p is the probe frequency in Hz.

Figure 7 shows the convolution of two Doppler broadened absorptions for $|F = 1\rangle \rightarrow |F'\rangle$ and $|F = 2\rangle \rightarrow |F'\rangle$. For theoretical modeling, we have taken the Doppler decoherence $\gamma_3 = 342$ along with total spontaneous decay of excited state $\Gamma_3 = \Gamma_{32} + \Gamma_{31} = 684$ MHz when dealing with line shapes inside any of the Doppler.

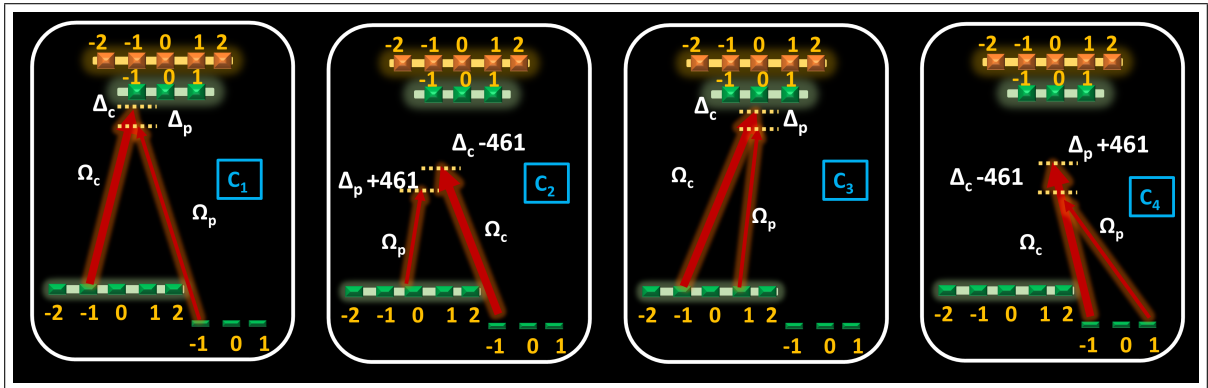


Figure 9: All four possible probe-control excitation configurations.

D Setting frequency reference

Doppler-free Saturated Absorption Spectroscopy [37] is performed using an independent vapor cell. The blue line in figure 8 shows the hyperfine transition lines where the strongest peak corresponds to $|F = 2\rangle \rightarrow |F'\rangle$ transition, the weakest peak corresponds to $|F = 1\rangle \rightarrow |F'\rangle$ transition and the middle dip is the crossover resonance in the spectroscopy of ^{39}K . The orange line shows a typical dark resonance. The separation between the two peaks in the spectroscopy refers to the ground hyperfine splitting as

$$|T_{|F=2\rangle \rightarrow |F'\rangle} - T_{|F=1\rangle \rightarrow |F'\rangle}| = 461.7\text{MHz} \quad (9)$$

From the above equation, all time scales from the oscilloscopes can be converted to frequency scale.

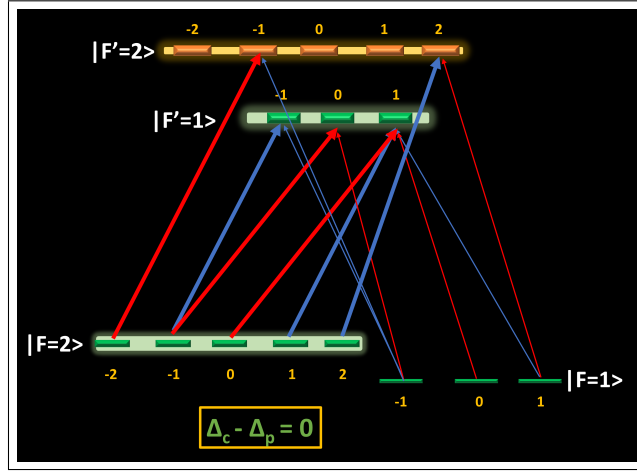


Figure 10: Demonstration of multiple Λ systems for two types of polarization of light. Blue lines are used for π polarized light and red lines are used for σ polarized light. Only a few Λ 's are shown here for clarity. (color online)

E Three line shapes

Lets denote the probe susceptibility in equation 8 as $\chi(\Delta_p, \Delta_c)$. Case C_1 is the standard case. For case C_2 , we can exchange the role of probe and control in the following way $\chi(\Delta_p, \Delta_c) \rightarrow \chi(\Delta_p + 461.7, \Delta_c - 461.7)$. This new configuration still satisfies the two-photon resonance condition. In the same argument, the susceptibility for case C_3 is $\chi(\Delta_p + 461.7, \Delta_c)$ and for case C_4 is $\chi(\Delta_p, \Delta_c - 461.7)$. Finally, the net absorption can be written as

$$\alpha_p = \sum_{i=1}^4 x_i \int_{v=-\infty}^{v=+\infty} \text{Im}(\chi)_i \mathcal{P}(v) dv \quad (10)$$

Here i is for case C_i and \mathcal{P} is the 1D Maxwell-Boltzmann velocity distribution given by

$$\mathcal{P} = \frac{1}{\sqrt{2\pi}D} e^{-\frac{v^2}{D^2}} \quad (11)$$

where $D = \sqrt{\frac{2k_B T}{m}}$ is the most probable velocity. Figure 9 depicts all four cases.

F Contribution of all possible Λ -system due to magnetic sub levels

Apart from having four different case as shown in figure 9, there are multiple Λ systems possible within a given case due to the existence of near-degenerate magnetic sub-levels of each hyperfine states. Considering the configuration of case C_1 , few Λ 's are shown in figure 10 where we use blue lines for linear polarized light and red lines for circular polarized light. Since we use linear polarization in our experiment, and a linear polarization state is a combination of right and left circular polarizations, all types of probe and control polarization choices need to be taken into account such as $Probe(\pi) - Control(\pi)$, $Probe(\sigma^+) - Control(\sigma^+)$, $Probe(\sigma^-) - Control(\sigma^-)$, $Probe(\pi) - Control(\sigma^+)$, $Probe(\pi) - Control(\sigma^-)$, $Probe(\sigma^+) - Control(\pi)$, $Probe(\sigma^-) - Control(\pi)$, $Probe(\sigma^+) - Control(\sigma^-)$ and $Probe(\sigma^-) - Control(\sigma^+)$. The Rabi frequencies (Ω_p, Ω_c) are scales as $\Omega_c \rightarrow s\Omega_c$ and $\Omega_p \rightarrow s'\Omega_p$ when adding contributions where s and s' are the Clebs Gordon co-efficient [38] for the respective transitions. However, there is no significant difference in line shape and positions after considering all the possible Λ 's within a given case.

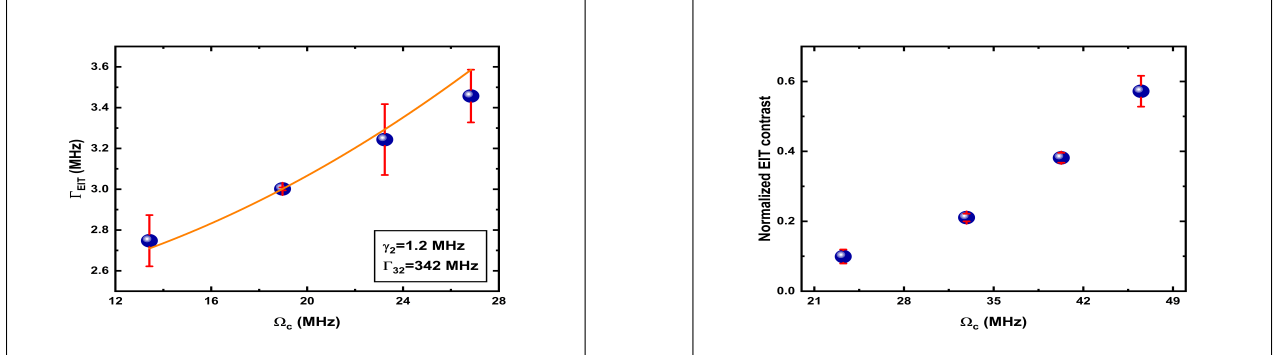


Figure 11: (Left) EIT line width is plotted against control Rabi frequency Ω_c with error bars. The blue-filled circles are experimental data points and the orange solid line is the theoretical fit. (Right) EIT contrast is plotted against Ω_c with error bars. (color online)

G EIT line width characteristics

At $\Delta_c = -923.4$, EIT features are recorded for case C_1 for various values of control power. The Gaussian background is subtracted and a Lorentzian fit is performed. Figure 11 shows the line width and contrast variation with control Rabi frequency Ω_c . The contrast increases with Ω_c at the expense of broader line width. By rearranging the imaginary part of probe susceptibility, we can read off the EIT line width

$$\Gamma_{EIT} = 2\left[\gamma_2 + \frac{\Omega_c^2}{\sqrt{OD}\Gamma_{32}}\right] \quad (12)$$

Here OD is the optical density at temperature T. The expression to calculate OD [39] is given by

$$OD = \frac{n\omega_p|d_{13}|L}{\epsilon_0 c \hbar (\Gamma_{31} + \Gamma_{32})} \quad (13)$$

In the above equation, $n = 2.3 \times 10^{10}$ atoms/cc is the atomic density at cell temperature $T = 60^\circ\text{C}$, $\omega_p = 391.016$ THz is the probe frequency in D_2 line, $|d_{13}| = 2.46 \times 10^{-29}$ C-m is the dipole matrix element [22], $L = 75$ mm is the cell length, ϵ_0 , \hbar , c are vacuum permittivity, reduced Planck's constant, velocity of light respectively and Γ_{31}, Γ_{32} are Doppler broadened spontaneous decay rates. The density at temperature T is calculated using [22]

$$\log p = 7.4077 - \frac{4453}{T} \quad (14)$$

H Acknowledgments

The authors thank Dr. Sanjukta Roy for insightful discussions. The authors also thank S. Majumder and A. Misra for their discussions and assistance. The authors also thank the RRI IT section and workshop.

References

- [1] Zbigniew Ficek and S Swain. *Quantum Interference and Coherence: Theory and Experiments*. Springer New York, NY, 01 2005.
- [2] Stephen E. Harris. Electromagnetically induced transparency. *Physics Today*, 50(7):36–42, Jul 1997.
- [3] Michael Fleischhauer, Atac Imamoglu, and Jonathan P. Marangos. Electromagnetically induced transparency: Optics in coherent media. *Rev. Mod. Phys.*, 77:633–673, Jul 2005.
- [4] Ran Finkelstein, Samir Bali, Ofer Firstenberg, and Irina Novikova. A practical guide to electromagnetically induced transparency in atomic vapor. *New Journal of Physics*, 25(3):035001, mar 2023.
- [5] Xihua Yang, Yuanyuan Zhou, and Min Xiao. Entangler via electromagnetically induced transparency with an atomic ensemble. *Scientific Reports*, 3(1):3479, Dec 2013.
- [6] John Kitching. Chip-scale atomic devices. *Applied Physics Reviews*, 5(3):031302, Aug 2018.
- [7] J. Vanier. Atomic clocks based on coherent population trapping: a review. *Applied Physics B*, 81(4):421–442, Aug 2005.
- [8] Lijun Ma, Oliver Slattery, and Xiao Tang. Optical quantum memory based on electromagnetically induced transparency. *Journal of Optics*, 19(4):043001, feb 2017.
- [9] H. H. Jen, Bo Xiong, Ite A. Yu, and Daw-Wei Wang. Electromagnetically induced transparency and slow light in quantum degenerate atomic gases. *J. Opt. Soc. Am. B*, 30(11):2855–2863, Nov 2013.
- [10] Shanchao Zhang, Shuyu Zhou, M. M. T. Loy, G. K. L. Wong, and Shengwang Du. Optical storage with electromagnetically induced transparency in a dense cold atomic ensemble. *Opt. Lett.*, 36(23):4530–4532, Dec 2011.

- [11] Chi Shu, Peng Chen, Tsz Kiu Aaron Chow, Lingbang Zhu, Yanhong Xiao, M. M. T. Loy, and Shengwang Du. Subnatural-linewidth biphotons from a doppler-broadened hot atomic vapour cell. *Nature Communications*, 7(1):12783, Sep 2016.
- [12] J. Soni, S. Mansha, S. Dutta Gupta, A. Banerjee, and N. Ghosh. Giant goos-hänchen shift in scattering: the role of interfering localized plasmon modes. *Opt. Lett.*, 39(14):4100–4103, Jul 2014.
- [13] Xiao-Jun Zhang, Hai-Hua Wang, Zhi-Peng Liang, Yan Xu, Cun-Bo Fan, Cheng-Zhi Liu, and Jin-Yue Gao. Goos-hänchen shift in a standing-wave-coupled electromagnetically-induced-transparency medium. *Phys. Rev. A*, 91:033831, Mar 2015.
- [14] R. Thomas, C. Kupchak, G. S. Agarwal, and A. I. Lvovsky. Observation of electromagnetically induced transparency in evanescent fields. *Opt. Express*, 21(6):6880–6888, Mar 2013.
- [15] A. Sargsyan, C. Leroy, Y. Pashayan-Leroy, D. Sarkisyan, D. Slavov, and S. Cartaleva. Electromagnetically induced transparency and optical pumping processes formed in cs sub-micron thin cell. *Optics Communications*, 285(8):2090–2095, 2012.
- [16] Ichiro Yoshida, Nobuhito Hayashi, Kazuki Fujita, Shuya Taniguchi, Yoshitaka Hoshina, and Masaharu Mitsunaga. Line-shape comparison of electromagnetically induced transparency and raman ramsey fringes in sodium vapor. *Phys. Rev. A*, 87:023836, Feb 2013.
- [17] Fabien Bretenaker, Fabienne Goldfarb, Shikang Liu, Pascal Neveu, and Etienne Brion. Quantum optics in a metastable helium vapor. In Jacob Scheuer and Selim M. Shahriar, editors, *Optical and Quantum Sensing and Precision Metrology II*, volume PC12016, page PC1201634. International Society for Optics and Photonics, SPIE, 2022.
- [18] K. Bencheikh, E. Baldit, S. Briaudeau, P. Monnier, J. A. Levenson, and G. Mélin. Slow light propagation in a ring erbium-doped fiber. *Opt. Express*, 18(25):25642–25648, Dec 2010.
- [19] A. Lazoudis, T. Kirova, E. H. Ahmed, L. Li, J. Qi, and A. M. Lyyra. Electromagnetically induced transparency in an open Λ -type molecular lithium system. *Phys. Rev. A*, 82:023812, Aug 2010.
- [20] H. Cheng, H. M. Wang, S. S. Zhang, P. P. Xin, J. Luo, and H. P. Liu. High resolution electromagnetically induced transparency spectroscopy of rydberg 87rb atom in a magnetic field. *Opt. Express*, 25(26):33575–33587, Dec 2017.
- [21] Silpa B. S., Shovan Kanti Barik, Saptarishi Chaudhuri, and Sanjukta Roy. Transition frequency measurement of highly excited rydberg states of 87rb for a wide range of principal quantum numbers. *Opt. Continuum*, 1(5):1176–1192, May 2022.
- [22] T. G. Tiecke. Properties of potassium. 2011.
- [23] D. A. Long, A. J. Fleisher, D. F. Plusquellic, and J. T. Hodges. Electromagnetically induced transparency in vacuum and buffer gas potassium cells probed via electro-optic frequency combs. *Opt. Lett.*, 42(21):4430–4433, Nov 2017.
- [24] A. Sargsyan, P. A. Petrov, T. A. Vartanyan, and D. Sarkisyan. Electromagnetically induced transparency in potassium vapors: Features and restrictions. *Optics and Spectroscopy*, 120(3):339–344, Mar 2016.

- [25] Silvia Gozzini, Andrea Fioretti, Alessandro Lucchesini, Luca Marmugi, Carmela Marinelli, Stoyan Tsvetkov, Sanka Gateva, and Stefka Cartaleva. Tunable and polarization-controlled high-contrast bright and dark coherent resonances in potassium. *Opt. Lett.*, 42(15):2930–2933, Aug 2017.
- [26] Supplementary material: Doppler-assisted quantum resonances through swappable excitation pathways in potassium vapor. Online, 2024. Available at [link or DOI].
- [27] O. S. Mishina, M. Scherman, P. Lombardi, J. Ortalo, D. Felinto, A. S. Sheremet, A. Bramati, D. V. Kupriyanov, J. Laurat, and E. Giacobino. Electromagnetically induced transparency in an inhomogeneously broadened Λ transition with multiple excited levels. *Phys. Rev. A*, 83:053809, May 2011.
- [28] Zhuo Ren Chen and Xue Mei Su. Asymmetrical spectra due to atomic coherence of neighboring excited levels. *The European Physical Journal D*, 67(7):138, Jul 2013.
- [29] E Brion, L H Pedersen, and K Mølmer. Adiabatic elimination in a lambda system. *Journal of Physics A: Mathematical and Theoretical*, 40(5):1033, jan 2007.
- [30] Indra Hang Subba, Ranjit Kumar Singh, Nayan Sharma, Souvik Chatterjee, and Ajay Tripathi. Understanding asymmetry in electromagnetically induced transparency for 87rb in strong transverse magnetic field. *The European Physical Journal D*, 74(7):136, Jul 2020.
- [31] Yong Wang, Miaojun Guo, Jinze Wu, Jinhong Liu, Xudong Yang, and Jinhong Li. Propagation of gaussian vortex beams in electromagnetically induced transparency media. *Opt. Express*, 30(24):43426–43438, Nov 2022.
- [32] J. Anupriya, Nibedita Ram, and M. Pattabiraman. Hanle electromagnetically induced transparency and absorption resonances with a laguerre gaussian beam. *Phys. Rev. A*, 81:043804, Apr 2010.
- [33] Sagar Sutradhar, Anirban Misra, Gourab Pal, Sayari Majumder, Sanjukta Roy, and Saptarishi Chaudhuri. Fast loaded dual species magneto optical trap of cold sodium and potassium atoms with light-assisted inter-species interaction. *AIP Advances*, 13(6):065317, 06 2023.
- [34] Kang Ying, Yueping Niu, Dijun Chen, Haiwen Cai, Ronghui Qu, and Shangqing Gong. Laser frequency offset locking via tripod-type electromagnetically induced transparency. *Appl. Opt.*, 53(12):2632–2637, Apr 2014.
- [35] L. Weller, K. S. Kleinbach, M. A. Zentile, S. Knappe, I. G. Hughes, and C. S. Adams. Optical isolator using an atomic vapor in the hyperfine paschen-back regime. *Opt. Lett.*, 37(16):3405–3407, Aug 2012.
- [36] Jacob B. Khurgin. Slow light in various media: a tutorial. *Adv. Opt. Photon.*, 2(3):287–318, Sep 2010.
- [37] L Mudarikwa, K Pahwa, and J Goldwin. Sub-doppler modulation spectroscopy of potassium for laser stabilization. *Journal of Physics B: Atomic, Molecular and Optical Physics*, 45(6):065002, mar 2012.
- [38] Rubidium 87 d line data. Online, 2023. Available at <https://steck.us/alkalidata/rubidium87numbers.pdf>.

- [39] Kenneth DeRose, Kefeng Jiang, Jianqiao Li, Macbeth Julius, Linzhao Zhuo, Scott Wenner, and Samir Bali. Producing slow light in warm alkali vapor using electromagnetically induced transparency. *American Journal of Physics*, 91(3):193–205, Mar 2023.